Research Article Vol. 2, No. 11 / 15 November 2019 / OSA Continuum 3141

Computational-imaging-based optical coherence tomography in time- and frequency-domain

MENGQI DU,[1,2,3] KJELD S. E. EIKEMA,[1,2] AND STEFAN WITTE[1,2,4]

[1]*Advanced Research Center for Nanolithography (ARCNL), Science Park 106, 1098 XG Amsterdam, The Netherlands*
[2]*LaserLaB, Department of Physics and Astronomy, Vrije Universiteit Amsterdam, De Boelelaan 1105, 1081 HV Amsterdam, The Netherlands*
[3]*m.du@arcnl.nl*
[4]*witte@arcnl.nl*

Abstract: A computational 3D imaging system is developed that enables polychromatic, depth-resolved, diffraction-limited imaging of semi-transparent objects. By combining coherent diffractive imaging (CDI) and optical coherence tomography (OCT), we reconstruct tomographic images of 3D objects from a set of wavelength- and phase-resolved diffraction patterns, using numerical methods to achieve image quality beyond the hardware limits of the optical systems used. We implement both time- and frequency-domain versions of full-field OCT systems, and for both versions we demonstrate fully lensless, as well as high-numerical-aperture configurations. We provide a comparison and overview of these different practical approaches to depth-resolved computational imaging. Furthermore, we demonstrate depth-resolved imaging of multilayer samples with an isotropic resolution in the μm range over a depth range that extends well beyond the depth-of-focus given by the numerical aperture of the imaging system.

1. Introduction: computational imaging in optical coherence tomography

Three-dimensional (3D) imaging techniques have provided many new insights in material and life science. For the last half century, the unprecedented development of 3D imaging technologies such as computed tomography, magnetic resonance imaging, and ultrasound imaging has changed our life in various aspects [1]. The development of similar 3D imaging capabilities operating at smaller length scales down to micrometers has also been a subject of considerable attention, as it brings the prospect of non-invasive cellular-level-resolution imaging, which may one day replace the need for invasive biopsies in some medical applications. The main 3D optical technique that has shown the potential to fulfill that promise is optical coherence tomography (OCT), which has drawn considerable attention and is already widely applied in medical sensing and diagnosis [2–7].

OCT is based on the principle of low coherence interferometry, measuring optical echoes inside a semi-transparent object through interferometric comparison with a reference beam from a broadband light source. It has several notable advantages for high-resolution imaging, including the ability for label-free imaging, background rejection in turbid media through coherence gating, and coherent amplification of weak sample beams from sensitive biological samples. As in all high-resolution volumetric imaging systems, OCT faces the challenge to achieve extended images at sufficiently high acquisition speed. Since the first point-scanning time-domain OCT (TDOCT) was introduced in 1991 [2], various speed-increasing measurement schemes have been demonstrated, including full-field TDOCT [8,9], point-scanning spectral-domain OCT (SDOCT), point-scanning and full-field swept-source OCT (SSOCT).

#372363 https://doi.org/10.1364/OSAC.2.003141
Journal © 2019 Received 15 Jul 2019; revised 28 Aug 2019; accepted 15 Oct 2019; published 4 Nov 2019

OSA CONTINUUM

One fascinating property that all realizations of OCT offer is the decoupling between transverse and axial resolution, as the axial resolution is determined by the bandwidth of the light source rather than the imaging optics. However, it is complicated to make full use of this advantage, as the depth-of-field (DoF) of a traditional OCT measurement is still limited by the numerical aperture (NA) of the imaging system, leading to a trade-off between transverse resolution and imaging depth. Computational post-processing methods have been proposed to correct for the defocus blurring by estimating the point spread function of the OCT system and applying deconvolution algorithms [10–12]. Another approach to mitigate the limited imaging depth is to adopt lensless or computational imaging techniques [13–16], where numerical refocus can be used for different depths inside a thick object. Moreover, the interferometric nature of OCT provides an excellent starting point for computational image reconstruction, as the phase of the light field is directly measured in a holographic scheme.

This concept of combining holographic methods and broadband illumination to achieve 3D imaging capabilities has been explored by several groups, starting out either from a holography viewpoint [17,18] or from an OCT-centered approach [19,20]. In most of these systems, an off-axis holography geometry was employed, which enables rapid extraction of the interferometric term, but at the expense of field-of-view. One challenge in computational OCT stems from the wavelength-dependence of wave propagation in the Fresnel regime: the different spectral components of a broadband light pulse will therefore each require a different amount of numerical propagation from the detector to achieve a focused image at a specific object depth. In this paper we discuss a set of computational methods for disentangling the information contained in the polychromatic diffraction patterns to retrieve a volumetric image of a 3D object. We introduce and compare methods for time-domain and frequency-domain/swept-source OCT implementations. We then proceed to show these methods experimentally, in both lensless and high-NA configurations. All these variations are combined in one versatile on-axis full-field OCT setup, allowing a direct comparison of the different methods and implementations. With this system, we demonstrate depth-resolved reconstruction of multi-layer samples, with an isotropic resolution at the 2-3 μm level.

2. Principles of computational OCT

2.1. Computational TDOCT

In conventional TDOCT, a reference mirror is scanned over the distance that matches the axial extent of the object. The depth distribution is attained by taking the advantage of the low temporal coherence property of broadband light sources. Specifically, interference signals only appear when the optical path length difference between the two arms is within the coherence length of the light source. In lensless TDOCT, spatially coherent broadband light sources are required, as the numerical propagation step requires a well-defined spatial phase profile across the object field-of-view. However, each spectral component of the object exit wave propagates differently to the detection plane [21], resulting in a wavelength-dependent interference pattern at the detector plane. The recorded full-field image is then the incoherent sum of all these individual spectral components. In this case, the function of the reference wave is not only that of coherence gating, but also assisting to encode the phase information of the diffracted object field in the interferograms.

The intensity of polychromatic interferograms as a function of time delay between the reference and the object can be expressed in the form

$$I(t) = \int \mid E_o(\omega)e^{i\varphi_o(\omega)} + E_r(\omega)e^{i(\varphi_r(\omega)+\omega t)} \mid^2 d\omega, \tag{1}$$

where $E_o(\omega)e^{i\varphi_o(\omega)}$ represents the diffracted field of the object and $E_r(\omega)e^{i\varphi_r(\omega)}$ is the reference field at the detector plane. They are also functions of 2D planes (x, y), which are omitted for

OSA CONTINUUM

clarity. The extra phase term ωt represents the time- and frequency-dependent phase delay between the reference and object field. The integration over the spectra results in the total intensity. For convenience, we expand the intensity into:

$$I(t) = \int [|E_o|^2 + |E_r|^2 + E_o(\omega)E_r^*(\omega)e^{i(\Delta\varphi(\omega)-\omega t)} + E_o^*(\omega)E_r(\omega)e^{-i(\Delta\varphi(\omega)-\omega t)}]d\omega, \quad (2)$$

where $\Delta\varphi(\omega) = \varphi_o(\omega) - \varphi_r(\omega)$ denotes the initial phase difference between the reference and the object signals. In a similar way to Fourier transform spectroscopy [22], a Fourier transform is performed on the intensity signal along the time delay axis,

$$I(\omega) = \mathcal{F}_t\{I(t)\} = \bar{I}\delta(0) + E_o(\omega)E_r^*(\omega)e^{i\Delta\varphi(\omega)} + E_o^*(-\omega)E_r(-\omega)e^{i\Delta\varphi(-\omega)}. \quad (3)$$

Three terms are obtained in Eq. (3): these are the DC term (i.e. at $\omega = 0$), as well as two cross terms at positive and negative frequencies, which are complex conjugates of each other. The complex electric field information is contained in these individual cross terms, and a single cross term can be extracted from Eq. 3 through Fourier filtering (see e.g. [3]), resulting in:

$$I_{+1}(\omega, x, y) = E_o(\omega, x, y)E_r^*(\omega, x, y)e^{i\Delta\varphi(\omega, x, y)}. \quad (4)$$

For each location (x, y) on the detector, we obtain a complex spectrum, in which the intensity is the product of the amplitudes of the reference and object field, and the phase is the phase difference between them. If plane waves are used as reference, this complex field is proportional to the diffracted field of the object. In other words, we obtain the full information of the spectrally resolved diffraction fields of the object, both the amplitude and phase. Thus, numerical refocus can be readily done by using a bandwidth limited angular spectrum method [23], where each individual diffraction pattern is numerically propagated back to the object plane as

$$E_o(\omega, x_0, y_0) = \mathcal{P}\{E_o(\omega, x, y)E_r^*(\omega, x, y)e^{-i\Delta\varphi(\omega, x, y)}\}. \quad (5)$$

In order to retrieve the depth information, an inverse Fourier transform along the frequency axis back to the time domain is performed:

$$E_o(t, x_0, y_0) = \mathcal{F}_\omega^{-1}\{E_o(\omega, x_0, y_0)\}. \quad (6)$$

The time delay t is directly related to the axial position inside the object, as the reflected light from an axial position z relative to the reference mirror distance is given by $z = 2ct$. Thus the final result $E_o(t, x_0, y_0)$ in Eq. (6) provides the full three dimensional reconstruction of the object.

2.2. Computational SSOCT

In general, SSOCT collects equivalent data as TDOCT. The computational SSOCT reconstruction shares the same principle as TDOCT, except that it requires one more Fourier transform and the cross correlation term is selected out in the time domain. The data acquisition is performed in the frequency domain initially, as monochromatic interferograms are recorded as a function of optical wavelength or frequency:

$$I(\omega) = |E_o(\omega) + E_r(\omega)e^{-i\omega t_z}|^2, \quad (7)$$

where $t_z = z/c$ denotes the fixed time delay between the reference and the object. If the frequencies are sampled in an equi-spaced manner, a direct Fourier transform can be applied to Eq. (7), resulting in three separated terms in the time domain according to the following equation:

$$I(t) = \mathcal{F}_t\{I(\omega)\} = \bar{I}\delta(0) + \mathcal{F}_t\{E_o(\omega)E_r^*(\omega)\} \circledast \delta(t - t_z) + \mathcal{F}_t\{E_o^*(\omega)E_r(\omega)\} \circledast \delta(t + t_z). \quad (8)$$

The spacing between the zeroth order and the first order cross terms can be tuned by the time delay t_z. After selecting out one of the cross terms in the time domain, an inverse Fourier transform

OSA CONTINUUM

can be performed to transform back to the frequency domain, which leads to the same result as in the computational TDOCT (Eq. (4)), namely the full information of the diffracted fields from the object at each spectral component. Subsequently we can follow the same steps (Eq. (5–6)) as in TDOCT to reconstruct the 3D object.

3. Experimental setups and performance characterization

A key component in the experimental combination of OCT with lensless imaging is a spatially coherent broadband light source. A broadband supercontinuum white-light laser (NKT Photonics WhiteLase Micro, spectrum from 400 nm to 2000 nm, output power 200 mW) with a high degree of spatial coherence for all spectral components is used as shown in Fig. 1(a). Short-pass (1000 nm) and long-pass (700 nm) color filters are used to select part of the spectrum for our experiments. A polarizing beamsplitter cube is used to create two paths 1&2 and to provide polarized input for the acousto-optic tunable filter (AOTF, Gooch and Housego: TeO2 AOTF I-TF950-500-1-2-GH96) in path 2. After the polarizing beamsplitter cube, path 1 (dashed line) is for TDOCT, where the light beam is directed by mirrors M1, M2, and flip mirror FM into the telescope (1:12 magnification with a 50 μm pinhole at the common focal plane) for spatial filtering and collimation. Path 2 (solid line) is for SSOCT, where an AOTF is used to sweep through the spectrum. The AOTF has a broad tuning range from 700 nm to 1200 nm, with sub-nanometer spectral resolution at a maximum modulation speed of 100 kHz, allowing for fast acquisition. The sub-nm spectral resolution enables an imaging depth up to 1.6 mm in air. The zeroth order transmitted beam from the AOTF is blocked, and the first order beam is directed by mirror M3 and M4 into the telescope and spatial filter that was already described above. The main imaging part (dashed blue box) of the setup is based on a Michelson interferometer. The components in the gray box are for high NA settings, where an objective (Mitutoyo, M Plan Apo NIR 10x, 0.26 NA) and a tube lens (Thorlabs, TTL200) are arranged in a telecentric configuration to guarantee a plane wave illumination [24]. Both TDOCT and SSOCT can be performed in either lensless or high NA settings, depending on insertion of these components. For the TDOCT measurements, a reference mirror is mounted on a motorized stage (PI N-565 with controller E861, 13 mm travel range, 0.5 nm system resolution), which scans the time delay between the reference and the sample arms with evenly spaced steps in a stop and go configuration. The stabilization time of the stage for each step is roughly 100 ms. As the shortest wavelength used in the experiment is 700 nm, to fulfill Nyquist sampling and to take into account the double path in the reflection geometry, the biggest step size allowed is 175 nm. In our experiment 150 nm was chosen. At each step, a polychromatic interferogram is recorded by a 2D image sensor. Two different cameras have been used in the experiments, namely a Prosilica GT 3400 (Allied Vision Technology) with 3.69 μm pixel size and 3384*2704 pixels, and an ORCA-Flash 4.0 V3 (Hamamatsu), with 6.5 μm pixel size and 2048*2048 pixels. In the SSOCT measurements, the stage position is kept fixed, and spectral scanning is performed through electronic control of the AOTF. In these measurements, the camera is synchronized to the AOTF to record monochromatic interferograms at each wavelength.

To demonstrate 3D image reconstruction, multi-layer samples (Fig. 1(b)) are fabricated using UV lithography and thermal thin film deposition. Discrete structures are printed layer by layer using various metals, including gold, chromium, and germanium, with a thickness between 10 to 50 nm. In between different layers, photoresists (OrmoComp) are used as transparent media with a thickness ranging from 10 to 50 μm.

3.1. Transverse resolution

The transverse resolution (half pitch) of the computational OCT system is in principle limited by the diffraction limit of the imaging system, $\frac{\lambda}{2NA}$. In reality, the camera pixel size and dynamic range can become limiting factors if the spatial sampling of the Fresnel diffraction pattern is not

OSA CONTINUUM

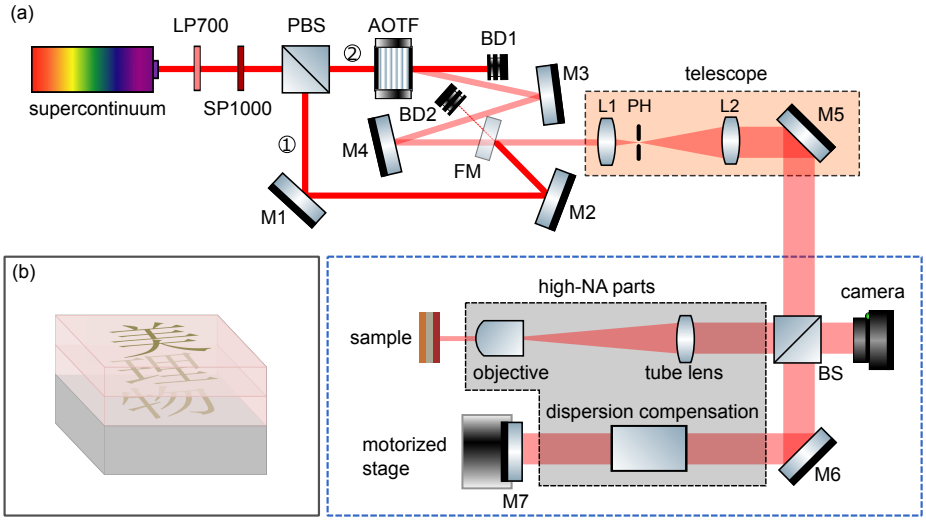

Fig. 1. (a) Schematic of the setup. LP700: 700 nm Long-pass filter, SP1000: 1000 nm short-pass filter, PBS: polarizing beamsplitter cube, AOTF: acousto-optic tunable filter, BS: beamsplitter cube, M: mirror, FM: flip mirror, BD: beam dump, L: lens, PH: pinhole. The setup has 4 different settings: low/high NA TDOCT and low/high NA SSOCT. The gray box contains the components for the high NA setting, consisting of an objective and a tube lens in the sample arm, and the dispersion compensation glass in the reference arm. (b) Schematic of a homemade 3-layer sample.

sufficient [25]. The simple lensless arrangement, featuring only free-space propagation from sample to detector, readily enables numerical aberration correction, but has a limited transverse resolution. To characterize the transverse resolution, we measured a 1951 USAF resolution target using the lensless TDOCT scheme (Fig. 1 without the high-NA parts in gray). An example of a measured polychromatic interferogram is shown in Fig. 2(a) and the 2D reconstruction is shown in Fig. 2(b) where the smallest resolved feature has a width of 11 μm (element 4 in group 5). In this case, the refocus distance from the camera plane to the object plane is 62 mm, which in principle leads to a detection NA of 0.08. With the central wavelength 780 nm, the diffraction limited resolution is 4.9 μm, which is a factor two lower than what is actually achieved. This discrepancy is mainly due to the limited dynamic range of the camera, leading to a reduced signal strength for the higher diffraction angles of the structure.

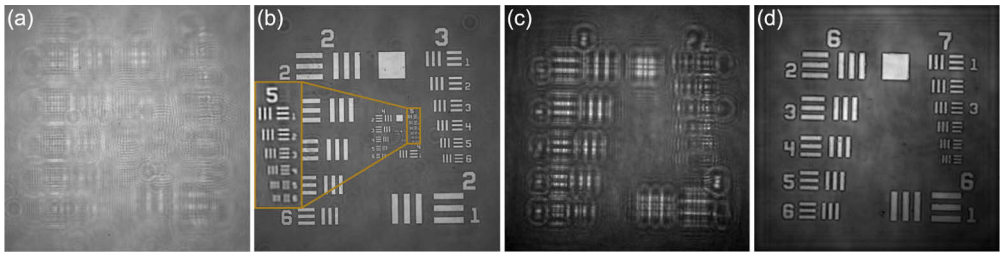

Fig. 2. Typical imaging results obtained with lensless OCT in different configurations. (a,b) Measurement and reconstruction of a USAF sample using the lensless TDOCT method. (c,d) Measurement and reconstruction of a USAF sample using the high-NA SSOCT method.

OSA CONTINUUM

In order to improve the transverse resolution, the high-NA optics is used as shown in Fig. 1(a). This increases the detection NA to 0.26, and at the same time the additional 10x magnification of the imaging system results in an effective sub-micron pixel size in the detected image (0.65 μm for the Hamamatsu camera, and 0.369 μm for the AVT). This makes it possible to achieve diffraction-limited resolution. The OCT measurements can be done either in the image plane or in an out-of-focus Fresnel diffraction plane. Figure 2(c) shows a high-NA measurement of the USAF target in the Fresnel regime, performed with SSOCT. After extracting the phase of the diffraction patterns at each wavelength using the methods described in the previous section, we numerically refocus the sample in Fig. 2(d). The smallest element (element 6 in group 7) on the USAF target is well resolved, demonstrating a transverse resolution better than 2.2 μm.

3.2. Axial resolution

Similar to traditional OCT, the axial resolution of our imaging systems are determined by the coherence length of the light source. The axial point spread function is mainly determined by the shape of the source spectrum, but dispersion differences between the reference and sample arm need to be compensated as well to achieve optimum depth resolution. Gaussian shaped spectra are considered ideal for not having side lobes in the axial response. The axial resolution is inversely proportional to the bandwidth of the spectrum, given by $R_z = \frac{2ln2}{\pi}\frac{\lambda_0{}^2}{\Delta\lambda}$, where λ_0 is the central wavelength and $\Delta\lambda$ is the full width at half maximum (FWHM) of the Gaussian spectrum [26]. However, most broadband light sources do not have smooth Gaussian spectra, thus spectral shaping before and after data acquisition have both been studied [27–30]. Numerical spectral shaping in the post-processing step has the advantage that it also accounts for the spectral response of optical components and detector. Besides Gaussian spectra, other spectral shapes have been proposed to improve axial resolution, including flat, Hamming-windowed, as well as adaptively shaped spectra for sidelobe reduction [31,32]. In our case, the complex spectrum of the backscattered light recorded by the camera can be calculated by Eq. 4, directly enabling post-processing spectral shaping. With a desired shape, for instance a super-Gaussian spectrum, we calculate the ratio between the original resolved spectrum and the desired spectrum to obtain a correction curve. In Fig. 3(a), the resolved spectrum from a USAF target measurement (using high-NA SSOCT), together with the assigned super-Gaussian shape is presented. The corresponding axial responses for the direct source spectrum, the super-Gaussian filtered spectrum, and the dispersion-compensated filtered spectrum are plotted in Fig. 3(c). It can be seen that the raw broadened, noisy axial response (blue trace) is only slightly improved after the spectral shaping (orange trace), and that the main improvement comes from the numerical dispersion compensation as will be further discussed below.

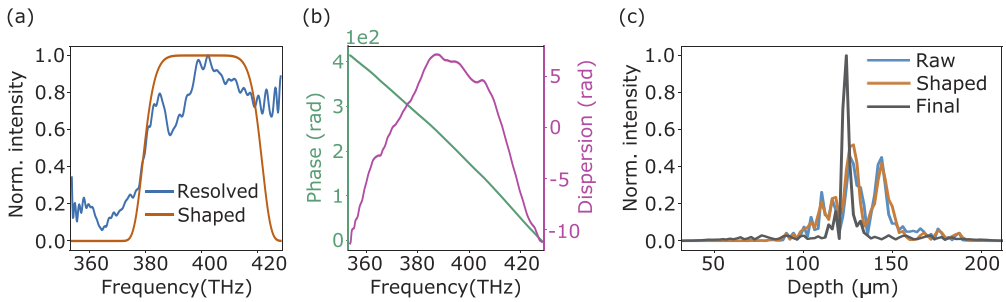

Fig. 3. A USAF sample measured by high-NA SSOCT method: (a) Resolved spectrum and final shaped spectrum. (b) Averaged phase (left axis) and extracted dispersion (right axis). (c) Axial response from the raw data, after spectral shaping and after dispersion compensation (final).

OSA CONTINUUM

The main obstacle for getting an optimal axial resolution in our system is chromatic dispersion. When light of a broad spectral range passes through an asymmetric interferometer that has different amounts of dispersive materials in the two arms, a spectrally dependent phase mismatch between the light fields from the two arms is induced. This is a common problem in traditional OCT, causing a deterioration of the achievable axial resolution. In order to achieve Fourier-limited axial resolution, both hardware- and software-based dispersion compensation methods have been proposed. Choosing identical optics or adding dispersive materials to physically match the optical materials in the two arms of the interferometer can compensate for non-sample induced dispersion [33,34]. Theoretical modeling of dispersion from specific samples, e.g. human eyes, has been applied to obtain optimal axial resolution [35,36]. Additionally, iterative optimization based on the sharpness of the image has been demonstrated [37,38], as well as numerical dispersion control to increase the axial range in frequency-domain OCT [39,40]. The interferometric OCT measurement scheme directly provides the phase information in the spectral domain (Eq. (4)), facilitating numerical dispersion compensation. The measured phase difference $\Delta\varphi(\omega)$ between the backscattered object field and reference field can be expanded into a Taylor series [41]:

$$\Delta\varphi(\omega) = \varphi(\omega_0) + \left.\frac{d\Delta\varphi}{d\omega}\right|_{\omega_0}(\omega-\omega_0) + \frac{1}{2}\left.\frac{d^2\Delta\varphi}{d\omega^2}\right|_{\omega_0}(\omega-\omega_0)^2 + \cdots , \tag{9}$$

where the zeroth-order term $\varphi(\omega_0)$ is a constant phase term at frequency ω_0, and the first-order term (the group delay) represents the linear phase difference due to the global optical path delay between the reference and the object. The longer the delay, the steeper the slope of the phase $\frac{d\Delta\varphi}{d\omega}$. The second- and higher-order terms are referred to as the dispersion terms that lead to broadening and distortion of the axial resolution, and any (numerical) dispersion compensation scheme aims to minimize these terms. In our lensless arrangement, direct characterization of dispersion is done by fitting a linear function to the resolved phase along the frequency axis and calculating the residual. In the high-NA arrangement, a combination of software- and hardware-based compensation is required, as the dispersion caused by the objective and tube lens in the sample arm is so severe that the first order interference signals extend well beyond the axial measurement range. Thus, prior to the numerical compensation, dispersive glass is added in the reference arm to reduce the dispersion to a level where extraction of the interferometric cross-term (Eq. 4) is feasible. In Fig. 3(b) we show the resolved phase and dispersion from the USAF sample measurement. The final axial response after both spectral shaping and dispersion compensation is plotted in Fig. 3(c), where 3.5 μm axial resolution in air is achieved. Considering that the DoF of the high NA system is 12 μm, the achieved axial resolution is more than 3 times better. Note that this short DoF would severely limit the axial measurement range in traditional OCT. In contrast, the numerical refocusing capability of computational OCT allows the use of such a high-NA configuration while maintaining the axial range set by the spectral resolution of the measurement system, without loss of transverse resolution outside the DoF.

4. Experimental results on computational 3D imaging

In the previous section we discussed characterization measurements on a single-layer USAF sample using different combinations of low- and high-NA, TDOCT and SSOCT to benchmark the achievable resolution. As a next step, reconstructions of home-made lithographic multi-layer samples are presented, and the performance of TDOCT and SSOCT is compared. As a first experiment, a homemade two-layer sample is measured in the low-NA lensless TDOCT arrangement, where a stack of polychromatic diffraction patterns is recorded during the data acquisition. In Fig. 4(a), the interference between the diffracted fields from the sample and the reference fields is shown. After numerical reconstruction, two different structures separated in depth are resolved, which are shown in Figs. 4(b) and 4(c), respectively. Due to the opacity of the

OSA CONTINUUM

top layer (consisting of 50 nm thick gold), a shadow is projected on the bottom layer tomogram. For comparison, the optical microscope image of the sample is shown in Fig. 4(d), where both layers are shown at the same time. The second row of Fig. 4 shows the reconstruction of another two-layer sample with smaller feature size measured in the high-NA TDOCT arrangement. Following the same reconstruction procedure, 2 μm features are resolved.

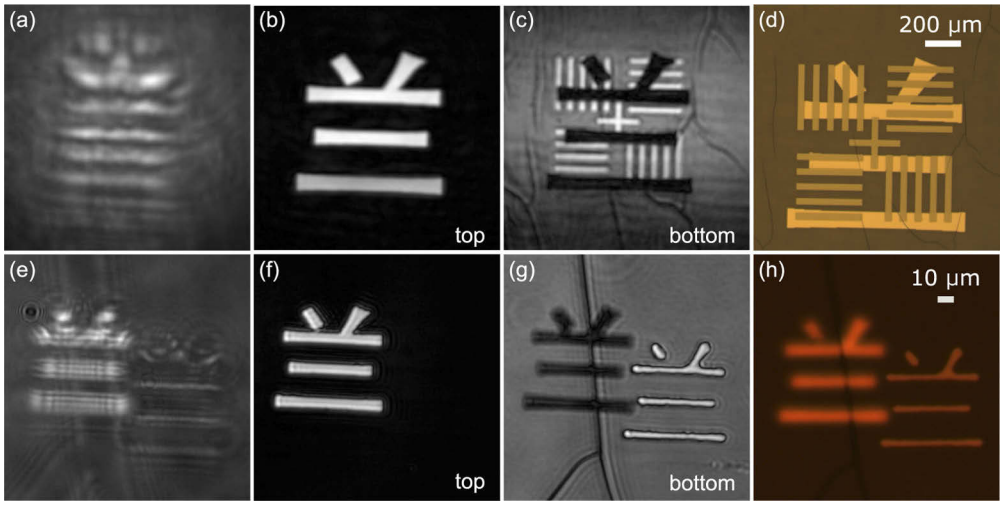

Fig. 4. Row 1: Measurement of a two-layer sample in the low-NA TDOCT configuration. Row 2: Measurement of a different two-layer sample with smaller features (in order to show the improved transverse resolution) in the high-NA TDOCT configuration. (a) A raw camera frame from the stack of polychromatic interferogram measurements. (b,c) Reconstructed tomograms of the top and bottom layers of the sample. (d) Optical microscope image (5x, 0.13 NA) of the sample. The scale bar specifies the transverse dimension of the two-layer sample. The axial separation of the two layers is 26 μm. (e) A raw camera frame from the stack of polychromatic interferogram measurements. (f,g) Reconstructed tomograms of the top and bottom layers of the sample. (h) Optical microscope image (10x, 0.25 NA) of the sample. The scale bar specifies the transverse dimension of the two-layer sample. The axial separation of the two layers is 28 μm.

As a first characterization of the SSOCT method, the reconstruction of a homemade three-layer sample measured in the high-NA arrangement is shown in Fig. 5. The three-layer sample is placed outside the focal plane of the objective. As can be seen in Fig. 5(a), all three-layer structures are out of focus. The resolved depth distribution of the whole sample, after the dispersion compensation and spectral shaping, is plotted in Fig. 5(b). In this graph the depth axis corresponds to the physical distance of the sample, which is converted from the direct result of optical distance while taking into account the double pass in the reflection geometry and the refractive index of the sample. From this measurement a depth resolution of 2.3 μm (FWHM) in the sample is obtained, and the physical distance between adjacent layers is measured to be 15 μm, which agrees with the expectation from the fabrication procedure. Figures 5(c) and 5(g) are the optical microscopy images taken from both sides of the sample, where the structure on the middle layer is not recognizable. In contrast, reconstructed tomograms of all three layers of the sample as measured with computational OCT are shown in Figs. 5(d-f) respectively. The structured layers in this three-layer sample are made of 10 nm thick layers of Germanium, which are semi-transparent in the near-infrared range. Therefore, the shadowing effect that is visible in the reconstructions shown in Fig. 4 is much less apparent in the middle (c) and bottom (d) layer reconstruction for this object. In these high-NA measurements, the axial extent of the sample

OSA CONTINUUM

is larger than the DoF of the system. Therefore, numerical refocusing is done for each layer separately to obtain focused images of the individual layers. In Fig. 5(h-j) we show the three-layer reconstruction when only one focal distance (for the bottom layer of the sample Fig. 5(f,j)) is chosen. The defocus effect in the middle layer (Fig. 5(i)) and the top layer (Fig. 5(h)) can be observed.

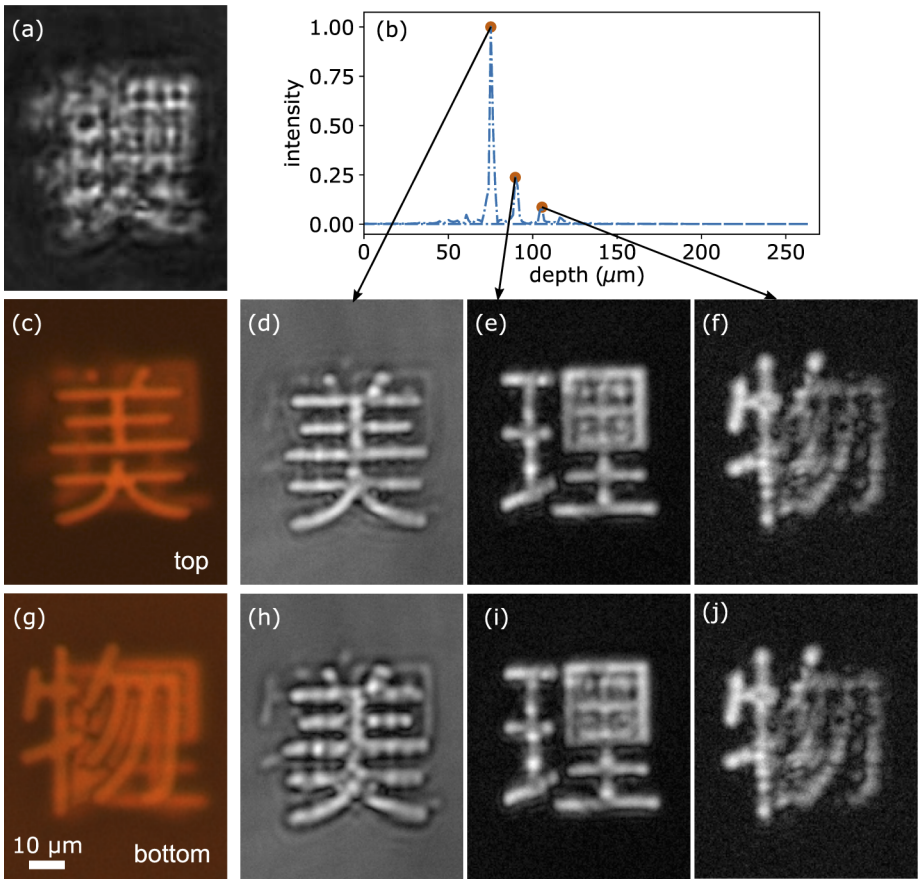

Fig. 5. (a) A single camera frame taken from a high-NA SSOCT measurement series. (b) Resolved depth distribution of the three-layer sample. (c, g) Optical microscope image (10x, 0.25 NA) of the three-layer sample from the front and back sides. The scale bar specifies the transverse dimension of the three-layer sample. The separation between adjacent layers is 15 μm. The 3D rendering of the sample is shown in Fig. 1(b). Reconstructed tomograms of the three layers of the sample with (d-f) and without (h-j) numerical refocusing for each individual layer.

To enable a direct comparison, the same three-layer sample is also measured in the high-NA TDOCT arrangement. Eight hundred images are recorded covering a scanning range of 120 μm in air (corresponding to 80 μm in the sample). Due to the limited speed of the scan stage, the data acquisition takes about 60 seconds, which is more than 10 times slower than the acquisition time in SSOCT, where 400 images are recorded during a wavelength scan from 700 nm to 850 nm. Due to the fast AOTF sweeping, in SSOCT the speed limitation is the camera (max 100 fps), while in TDOCT the main limitation is the time required for accurate stage positioning. In fact, in our present setting the SSOCT measurement covers a 3 times larger depth range within

OSA CONTINUUM

the aforementioned measurement time, so that the difference in data acquisition speed actually reaches a factor 30.

The resolved depth resolution in TDOCT is 2.3 μm, which is the same as in SSOCT within the experimental accuracy (see Fig. 6(a, b)). The resolved positions of the peaks are all relative to the starting position of the reference, so the absolute numbers in terms of depth can be different. The peak width and the relative distance between the peaks as measured with the two different methods are both in good agreement. The total incident energy on the sample integrated over the duration of the scan was 17 μJ and 31 μJ for TDOCT and SSOCT respectively. At these energies the final signal to noise ratio (SNR) in TDOCT is 3 dB lower than in SSOCT, which is directly explained by the difference in energy on sample. For further comparison, a series of simulations has been performed to investigate the noise sensitivity of the respective methods (Fig. 6(c, d)). From these simulations we find that the influence of the background signal, which is less than 5% of the maximum signal level in our measurements, has a limited effect on the SNR in both cases. However, in principle TDOCT is more sensitive to the noise from the detection side compared to SSOCT, because in the latter case any randomly distributed noise will be filtered by the additional Fourier transform [42,43]. This can be seen in Figs. 6(c) and 6(d), where 30% noise is added in the simulation on a two-layer object in both TDOCT and SSOCT. The noise floor is significantly increased for the case of TDOCT, while the SNR for the SSOCT reconstruction is only slightly affected.

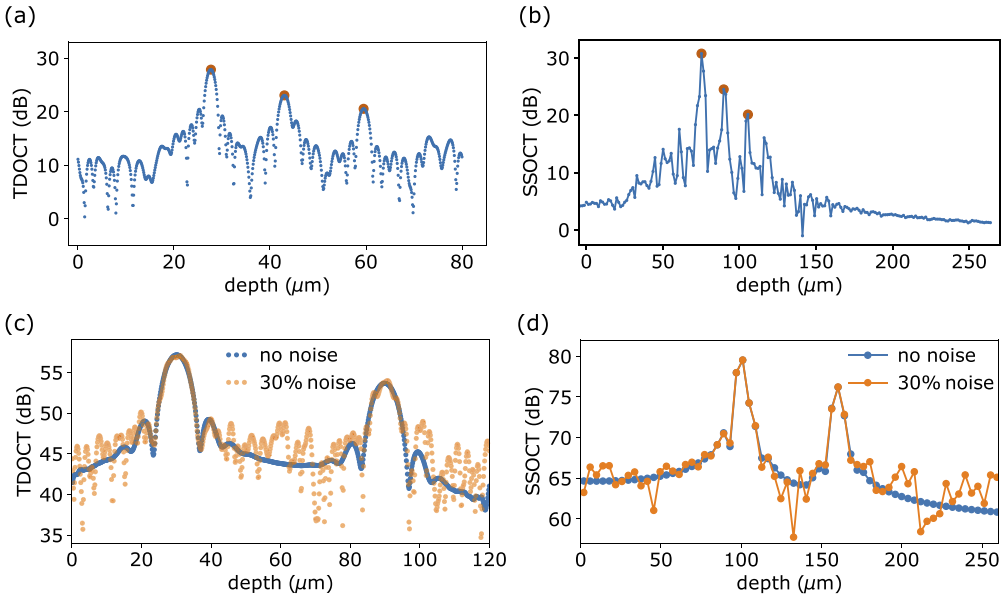

Fig. 6. Experimentally determined depth distribution of the three-layer sample measured with (a) high-NA TDOCT and (b) high-NA SSOCT on a logarithmic scale. (c,d) Simulated depth response with 30% noise added, and without noise on a two-layer object.

5. Conclusions

We have shown a comprehensive comparison of computational full-field OCT methods for tomographic reconstruction of 3D objects. In a single setup, we have combined low- and high-NA imaging systems as well as time-domain and swept-source OCT configurations, enabling a direct comparison of these different methods in terms of achievable resolution, depth range, measurement speed and noise sensitivity. Using this system, we show the advantage of computational imaging

OSA CONTINUUM

methods in OCT to enable high-NA transverse imaging combined with a large depth range that extends well beyond the DoF of the imaging hardware. The lensless (low-NA) arrangement allows for a simple and flexible experimental setup, but has a limited transverse resolution. A significant resolution improvement is provided by incorporating high-NA optics, which does require additional effort in dispersion balancing in the setup. With a homemade three-layer sample, we demonstrate a 3D reconstruction with 2 μm transverse and 3.5 μm axial resolution, and a measurement depth range of >200 μm.

Funding

European Research Council (ERC Starting grant nr. 637476); Nederlandse Organisatie voor Wetenschappelijk Onderzoek (NWO project 13934).

Disclosures

The authors declare no conflicts of interest.

References

1. A. Webb, *Introduction to biomedical imaging* (Wiley-IEEE Press, 2003).
2. D. Huang, E. Swanson, C. Lin, J. Schuman, W. Stinson, W. Chang, M. Hee, T. Flotte, K. Gregory, and C. Puliafito, "Optical coherence tomography," Science **254**(5035), 1178–1181 (1991).
3. A. F. Fercher, "Optical coherence tomography," J. Biomed. Opt. **1**(2), 157–173 (1996).
4. W. Drexler and J. G. Fujimoto, *Optical coherence tomography: technology and applications* (Springer Science & Business Media, 2008).
5. O. Assayag, M. Antoine, B. Sigal-Zafrani, M. Riben, F. Harms, A. Burcheri, K. Grieve, E. Dalimier, B. L. C. de Poly, and C. Boccara, "Large field, high resolution full-field optical coherence tomography: A pre-clinical study of human breast tissue and cancer assessment," Technol. Cancer Res. & Treat. **13**, 455–468 (2013).
6. R. F. Spaide, J. M. Klancnik, and M. J. Cooney, "Retinal vascular layers imaged by fluorescein angiography and optical coherence tomography," JAMA Ophthalmol. **133**(1), 45–50 (2015).
7. J. P. Campbell, M. Zhang, T. S. Hwang, S. T. Bailey, D. J. Wilson, Y. Jia, and D. Huang, "Detailed vascular anatomy of the human retina by projection-resolved optical coherence tomography angiography," Sci. Rep. **7**(1), 42201 (2017).
8. E. Beaurepaire, A. C. Boccara, M. Lebec, L. Blanchot, and H. Saint-Jalmes, "Full-field optical coherence microscopy," Opt. Lett. **23**(4), 244–246 (1998).
9. A. Dubois, K. Grieve, G. Moneron, R. Lecaque, L. Vabre, and C. Boccara, "Ultrahigh-resolution full-field optical coherence tomography," Appl. Opt. **43**(14), 2874–2883 (2004).
10. T. S. Ralston, D. L. Marks, P. Scott Carney, and S. A. Boppart, "Interferometric synthetic aperture microscopy," Nat. Phys. **3**(2), 129–134 (2007).
11. Y. Liu, Y. Liang, G. Mu, and X. Zhu, "Deconvolution methods for image deblurring in optical coherence tomography," J. Opt. Soc. Am. A **26**(1), 72–77 (2009).
12. Y.-Z. Liu, F. A. South, Y. Xu, P. S. Carney, and S. A. Boppart, "Computational optical coherence tomography," Biomed. Opt. Express **8**(3), 1549–1574 (2017).
13. J. Miao, P. Charalambous, J. Kirz, and D. Sayre, "Extending the methodology of X-ray crystallography to allow imaging of micrometre-sized non-crystalline specimens," Nature **400**(6742), 342–344 (1999).
14. H. N. Chapman and K. A. Nugent, "Coherent lensless X-ray imaging," Nat. Photonics **4**(12), 833–839 (2010).
15. D. Gabor, "A new microscopic principle," Nature **161**(4098), 777–778 (1948).
16. M. Lee, O. Yaglidere, and A. Ozcan, "Field-portable reflection and transmission microscopy based on lensless holography," Biomed. Opt. Express **2**(9), 2721–2730 (2011).
17. L. Yu and M. K. Kim, "Wavelength-scanning digital interference holography for tomographic three-dimensional imaging by use of the angular spectrum method," Opt. Lett. **30**(16), 2092–2094 (2005).
18. G. Sheoran, S. Dubey, A. Anand, D. S. Mehta, and C. Shakher, "Swept-source digital holography to reconstruct tomographic images," Opt. Lett. **34**(12), 1879–1881 (2009).
19. D. Hillmann, C. Lührs, T. Bonin, P. Koch, and G. Hüttmann, "Holoscopy-holographic optical coherence tomography," Opt. Lett. **36**(13), 2390–2392 (2011).
20. D. Hillmann, G. Franke, C. Lührs, P. Koch, and G. Hüttmann, "Efficient holoscopy image reconstruction," Opt. Express **20**(19), 21247–21263 (2012).
21. J. W. Goodman, *Introduction to Fourier optics* (Roberts and Company Publishers, 2005).
22. R. Bell, *Introductory Fourier transform spectroscopy* (Elsevier, 2012).
23. K. Matsushima and T. Shimobaba, "Band-limited angular spectrum method for numerical simulation of free-space propagation in far and near fields," Opt. Express **17**(22), 19662–19673 (2009).

OSA CONTINUUM

24. D. L. Marks, T. S. Ralston, S. A. Boppart, and P. S. Carney, "Inverse scattering for frequency-scanned full-field optical coherence tomography," J. Opt. Soc. Am. A **24**(4), 1034–1041 (2007).
25. D. W. E. Noom, D. E. Boonzajer Flaes, E. Labordus, K. S. E. Eikema, and S. Witte, "High-speed multi-wavelength Fresnel diffraction imaging," Opt. Express **22**(25), 30504 (2014).
26. C. Akcay, P. Parrein, and J. P. Rolland, "Estimation of longitudinal resolution in optical coherence imaging," Appl. Opt. **41**(25), 5256–5262 (2002).
27. A. C. Akcay, J. P. Rolland, and J. M. Eichenholz, "Spectral shaping to improve the point spread function in optical coherence tomography," Opt. Lett. **28**(20), 1921–1923 (2003).
28. W. Drexler, "Ultrahigh-resolution optical coherence tomography," J. Biomed. Opt. **9**(1), 47–75 (2004).
29. E. D. J. Smith, S. C. Moore, N. Wada, W. Chujo, and D. D. Sampson, "Spectral domain interferometry for ocdr using non-gaussian broad-band sources," IEEE Photonics Technol. Lett. **13**(1), 64–66 (2001).
30. R. Tripathi, N. Nassif, J. S. Nelson, B. H. Park, and J. F. de Boer, "Spectral shaping for non-gaussian source spectra in optical coherence tomography," Opt. Lett. **27**(6), 406–408 (2002).
31. D. L. Marks, P. S. Carney, and S. A. Boppart, "Adaptive spectral apodization for sidelobe reduction in optical coherence tomography images," J. Biomed. Opt. **9**(6), 1281–1287 (2004).
32. J. Gong, B. Liu, Y. L. Kim, Y. Liu, X. Li, and V. Backman, "Optimal spectral reshaping for resolution improvement in optical coherence tomography," Opt. Express **14**(13), 5909–5915 (2006).
33. C. K. Hitzenberger, A. Baumgartner, W. Drexler, and A. F. Fercher, "Dispersion effects in partial coherence interferometry: implications for intraocular ranging," J. Biomed. Opt. **4**(1), 144–152 (1999).
34. L. Vabre, A. Dubois, and A. C. Boccara, "Thermal-light full-field optical coherence tomography," Opt. Lett. **27**(7), 530–532 (2002).
35. A. F. Fercher, W. Drexler, C. K. Hitzenberger, and T. Lasser, "Optical coherence tomography - principles and applications," Rep. Prog. Phys. **66**(2), 239–303 (2003).
36. A. Federici and A. Dubois, "Full-field optical coherence microscopy with optimized ultrahigh spatial resolution," Opt. Lett. **40**(22), 5347–5350 (2015).
37. D. L. Marks, A. L. Oldenburg, J. J. Reynolds, and S. A. Boppart, "Autofocus algorithm for dispersion correction in optical coherence tomography," Appl. Opt. **42**(16), 3038–3046 (2003).
38. M. Wojtkowski, V. J. Srinivasan, T. H. Ko, J. G. Fujimoto, A. Kowalczyk, and J. S. Duker, "Ultrahigh-resolution, high-speed, fourier domain optical coherence tomography and methods for dispersion compensation," Opt. Express **12**(11), 2404–2422 (2004).
39. S. Witte, M. Baclayon, E. J. Peterman, R. F. Toonen, H. D. Mansvelder, and M. L. Groot, "Single-shot two-dimensional full-range optical coherence tomography achieved by dispersion control," Opt. Express **17**(14), 11335 (2009).
40. B. Hofer, B. Považay, B. Hermann, A. Unterhuber, G. Matz, and W. Drexler, "Dispersion encoded full range frequency domain optical coherence tomography," Opt. Express **17**(1), 7–24 (2009).
41. A. Weiner, *Ultrafast optics*, vol. 72 (John Wiley & Sons, 2011).
42. J. F. de Boer, B. Cense, B. H. Park, M. C. Pierce, G. J. Tearney, and B. E. Bouma, "Improved signal-to-noise ratio in spectral-domain compared with time-domain optical coherence tomography," Opt. Lett. **28**(21), 2067–2069 (2003).
43. R. Leitgeb, C. K. Hitzenberger, and A. F. Fercher, "Performance of fourier domain vs. time domain optical coherence tomography," Opt. Express **11**(8), 889–894 (2003).